

# Robust Localization in OFDM-Based Massive MIMO through Phase Offset Calibration

Qing Zhang\*, Adham Sakhnini\*,†, Robbert Beerten\*, Haoqiu Xiong\*,  
Zhuangzhuang Cui\*, Yang Miao#, and Sofie Pollin\*,†

\*Department of Electrical Engineering (ESAT), KU Leuven, Belgium

#Department of Electrical Engineering (EEMCS-EE), University of Twente, The Netherlands

†Interuniversity Microelectronics Centre (IMEC), Leuven, Belgium

**Abstract**—Accurate localization in Orthogonal Frequency Division Multiplexing (OFDM)-based massive Multiple-Input Multiple-Output (MIMO) systems depends critically on phase coherence across subcarriers and antennas. However, practical systems suffer from frequency-dependent and (spatial) antenna-dependent phase offsets, degrading localization accuracy. This paper analytically studies the impact of phase incoherence on localization performance under a static User Equipment (UE) and Line-of-Sight (LoS) scenario. We use two complementary tools. First, we derive the Cramér-Rao Lower Bound (CRLB) to quantify the theoretical limits under phase offsets. Then, we develop a Spatial Ambiguity Function (SAF)-based model to characterize ambiguity patterns. Simulation results reveal that spatial phase offsets severely degrade localization performance, while frequency phase offsets have a minor effect in the considered system configuration. To address this, we propose a robust Channel State Information (CSI) calibration framework and validate it using real-world measurements from a practical massive MIMO testbed. The experimental results confirm that the proposed calibration framework significantly improves the localization Root Mean Squared Error (RMSE) from 5 m to 1.2 cm, aligning well with the theoretical predictions.

**Index Terms**—CSI calibration, CRLB, localization, massive MIMO, OFDM, phase offset, spatial ambiguity function

## I. INTRODUCTION

The rapid evolution of wireless communication systems has led to the widespread adoption of Orthogonal Frequency Division Multiplexing (OFDM) in conjunction with massive Multiple-Input Multiple-Output (MIMO) architectures. These systems promise high spatial resolution and corresponding robust localization, which empowers Integrated Sensing and Communication (ISAC) for next-generation wireless networks [1]–[3]. However, a critical issue has arisen from imperfect phase coherence across subcarriers and antenna elements due to hardware impairments.

In practice, OFDM systems inherently suffer from frequency-dependent phase distortions arising from hardware impairments such as oscillator drift, Carrier Frequency Offset (CFO), and IQ imbalance. Throughout the spatial dimension, antenna-dependent phase offsets due to hardware heterogeneity also lead to a severe degradation of signal coherence, thus undermining the overall performance of localization algorithms [4]–[6].

This work is supported by the EU-HORIZON-MSCA-2022-DN No. 101119652 (6<sup>th</sup>Sense), Horizon Europe Research and Innovation programme No. 101192521 (MultiX), and No. 101139257 (SUNRISE-6G).

Over the past decades, extensive research efforts have been dedicated to addressing phase synchronization challenges in multi-antenna and multi-carrier systems. Existing studies laid foundational techniques for frequency synchronization, notably Moose’s pioneering cyclic prefix-based frequency offset estimation method, widely applied to mitigate CFO in OFDM systems [7]. Subsequent advances introduced maximum likelihood estimators and least squares approaches, enhancing the accuracy and robustness of CFO compensation techniques [8]. More recently, studies have increasingly recognized the challenges introduced by spatial offsets inherent in massive MIMO architectures. Radhakrishnan et al. [4] and Studer et al. [5] highlighted significant localization performance degradation due to residual hardware impairments, particularly antenna-dependent phase variations. Shahmansoori et al. [3] emphasized the need for joint spatial-frequency synchronization strategies, integrating antenna calibration methods with channel estimation algorithms to improve localization precision. Despite these advancements, a comprehensive analysis of phase incoherence effects on localization performance with experimental validation remains limited, representing the research gap that this paper aims to address.

In this paper, we present a unified analytical and empirical study of phase incoherence in OFDM-based massive MIMO localization, using two complementary tools: Cramér-Rao Lower Bound (CRLB) and Spatial Ambiguity Function (SAF). We derive analytical expressions of the CRLB to reveal the mathematical optimal localization accuracy that the unbiased location estimator can achieve. Considering the CRLB does not take into account the global ambiguities that the phase offsets may cause, we develop a unified theoretical model based on the SAF and focus on sidelobe levels by defining a metric named Peak-to-Median Sidelobe Ratio (PMSR). To empirically validate our theoretical insights, we perform experimental measurements using a massive MIMO testbed and introduce a robust CSI calibration framework to compensate for frequency and spatial phase offsets in measured data. Experimental results demonstrate that our proposed calibration significantly improves the combination of coherent signals, thus greatly enhancing the localization performance.

The main contributions are summarized as follows:

- We introduce an analytical framework that leverages the CRLB and SAF, explicitly accounting for both frequency

and spatial phase offsets in OFDM-based massive MIMO systems, thus providing theoretical insights into phase incoherence effects on localization performance.

- We systematically simulate and analyze the effects of phase incoherence on localization performance through introducing the PMSR as a practical metric to quantify the ambiguity observed in SAFs under varying levels of phase incoherence.
- We propose a practical and effective CSI calibration framework that compensates for frequency and spatial phase offsets, enabling coherent signal combination across subcarriers and antennas.
- We validate the effectiveness of the proposed calibration approach through experimental measurements conducted on a real-world massive MIMO testbed, demonstrating a significant reduction of the localization RMSE (from meters to centimeter level) compared to uncalibrated scenarios.

**Scope and assumptions:** Throughout this paper, we assume a static single UE and LoS scenario. Multi-UE is not considered due to the limited range resolution (i.e., 16.67 m) of the validation testbed (Section V). Although the CRLB and SAF derivations assume only the LoS component for simplification, the observations remain valid in diffuse multipath where the non-LoS terms are zero-mean with independent phases. We have preliminary evidence of the generalizability of the proposed CSI calibration framework in a dynamic passive sensing scenario. A complete evaluation is outside this paper's scope and will be reported in our future work.

The remainder of this paper is structured as follows. Section II details the system model and the corresponding CRLB and SAF. Section III evaluates the CRLB under varying phase offsets. Section IV analyzes SAF simulations with a focus on PMSR trends. Section V provides experimental validation using a massive MIMO testbed in the real world. Finally, Section VI summarizes the key findings of the paper and discusses directions for future research.

## II. SYSTEM MODEL

### A. OFDM-Based Massive MIMO System Model

To analyze the impact of phase incoherence on localization performance, we consider the OFDM-based massive MIMO scenario depicted in Fig. 1. A static User Equipment (UE) transmits a predefined pilot signal to  $N$  receiver antennas arranged as a Uniform Linear Array (ULA). The signal received at each antenna differs according to its respective distance  $d_n$  from the UE. The received signal at the  $n$ -th antenna during a single OFDM symbol is expressed as:

$$r_{nk} = \alpha_n e^{-j2\pi(\frac{f_c}{c} + \frac{\Delta f}{c} k)d_n} + w_{nk}, \quad (1)$$

where  $k \in \{1, 2, \dots, K\}$  is the OFDM subcarrier index,  $\alpha_n$  denotes the signal amplitude accounting for path loss,  $f_c$  is the carrier frequency,  $\Delta f$  is the subcarrier spacing, and  $c$  is the speed of light.  $w_{nk}$  is the complex additive white Gaussian noise, and  $w_{nk} \sim \mathcal{CN}(0, \sigma_n^2)$ .

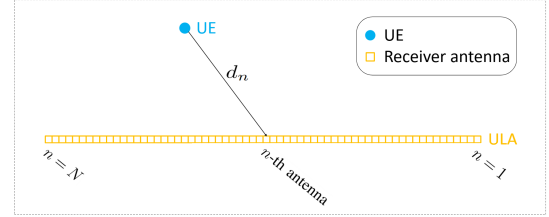


**Fig. 1:** Considered scenario: A static UE transmitting OFDM signals with  $K$  subcarriers to a ULA with  $N$  receiver antennas.

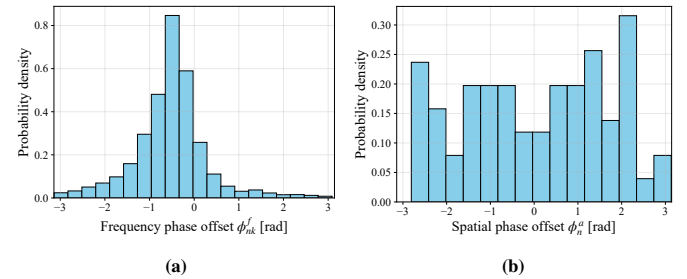


**Fig. 2:** Distributions of the frequency and spatial phase offsets from the measured data: (a) Frequency phase offset: Gaussian distribution. (b) Spatial phase offset: uniform distribution.

When frequency-dependent phase offset is present, an additional phase term  $\phi_{nk}^f$  is introduced. This offset is commonly modelled as a Gaussian distributed random variable:  $\phi_{nk}^f \sim \mathcal{N}(\mu_\phi, \sigma_\phi^2)$  [9]. As shown in Fig. 2(a), this Gaussian distribution is empirically validated using the data measured in Section V. Similarly, an antenna-dependent phase offset  $\phi_n^a$  is modelled as a uniform distribution:  $\phi_n^a \sim \mathcal{U}(-\Delta, \Delta)$ , with a standard deviation  $\sigma_\phi^a$ , as shown in Fig. 2(b). Consequently, the received signal in (1) becomes:

$$\tilde{r}_{nk} = \alpha_n e^{-j2\pi(\frac{f_c}{c} + \frac{\Delta f}{c} k)d_n} e^{j\phi_{nk}^f} e^{j\phi_n^a} + w_{nk}. \quad (2)$$

### B. Cramér-Rao Lower Bound

We respectively analyze the impacts of frequency and spatial phase offsets by deriving their corresponding analytical expressions of CRLB for estimating the UE location.

Define the unknown parameter vector as:

$$\boldsymbol{\eta} = [x \ y \ \phi]^T, \quad (3)$$

where  $(x, y)$  is the UE location,  $\phi = \{\phi_{nk}^f\}$  or  $\{\phi_n^a\}$ , depending on the considered phase offset. Then the full Fisher Information Matrix (FIM) with prior knowledge of  $\phi$  is structured as [10]:

$$\mathbf{J}_\eta = \begin{bmatrix} \mathbf{J}_{xy,xy} & \mathbf{J}_{xy,\phi} \\ \mathbf{J}_{\phi,xy} & \mathbf{J}_{\phi,\phi} \end{bmatrix}. \quad (4)$$

To marginalize the effect of  $\phi$ , an Effective FIM (EFIM) for  $\mathbf{p} = [x, y]^T$  is given by:

$$\mathbf{J}_{\text{eff}} = \mathbf{J}_{xy,xy} - \mathbf{J}_{xy,\phi} \cdot \mathbf{J}_{\phi,\phi}^{-1} \cdot \mathbf{J}_{xy,\phi}^T, \quad (5)$$

where:

$$\mathbf{J}_{xy,xy} = \frac{2}{\sigma_n^2} \sum_{n=1}^N \sum_{k=1}^K \Re \left\{ \frac{\partial \mu_{nk}}{\partial \mathbf{p}} \left( \frac{\partial \mu_{nk}}{\partial \mathbf{p}} \right)^H \right\}; \quad (6)$$

$$\mathbf{J}_{xy,\phi} = \frac{2}{\sigma_n^2} \sum_{n=1}^N \sum_{k=1}^K \Re \left\{ \frac{\partial \mu_{nk}}{\partial \mathbf{p}} \left( \frac{\partial \mu_{nk}}{\partial \phi} \right)^H \right\}, \quad (7)$$

and  $\Re \{\cdot\}$  denotes the real part of a complex number.  $\mu_{nk}$  is the expected value of the received signal,  $\mu_{nk} = \mathbb{E}(\tilde{r}_{nk})$ , with:

$$\frac{\partial \mu_{nk}}{\partial x} = -j2\pi \left( \frac{f_c}{c} + \frac{\Delta f}{c} k \right) \frac{x - x_n}{d_n} \mu_{nk}; \quad (8)$$

$$\frac{\partial \mu_{nk}}{\partial y} = -j2\pi \left( \frac{f_c}{c} + \frac{\Delta f}{c} k \right) \frac{y - y_n}{d_n} \mu_{nk}; \quad (9)$$

$$\frac{\partial \mu_{nk}}{\partial \phi_n^f} = j\mu_{nk} \quad \text{or} \quad \frac{\partial \mu_{nk}}{\partial \phi_n^a} = j\mu_{nk}. \quad (10)$$

Furthermore, in the case of  $\phi_{nk}^f$  with the Gaussian distribution:

$$\mathbf{J}_{\phi,\phi} = \frac{2}{\sigma_n^2} \text{diag}(|\mu_{nk}|^2) + \frac{1}{\sigma_\phi^2} \mathbf{I}_{NK}; \quad (11)$$

and for  $\phi_n^a$  with the uniform distribution:

$$\mathbf{J}_{\phi,\phi} = \frac{2}{\sigma_n^2} \text{diag} \left( \sum_{k=1}^K |\mu_{nk}|^2 \right) + \frac{3}{\Delta^2} \mathbf{I}_N. \quad (12)$$

Finally, we evaluate the Root Mean Squared Error (RMSE) of the location estimation as:

$$\text{CRLB}_{xy}^{\text{RMSE}} = \sqrt{\text{tr}(\text{CRLB}_{xy})} = \sqrt{\text{tr}(\mathbf{J}_{\text{eff}}^{-1})} \quad (13)$$

where the operator  $\text{tr}(\cdot)$  denotes the sum of the diagonal terms in  $\text{CRLB}_{xy}$ .

### C. Spatial Ambiguity Function and Performance Metric

We compare the SAFs in the three cases: ideal signal, signal with frequency phase offset, and signal with spatial phase offset. Using the ideally received signal defined in (1), the SAF is formulated as the matched filter output that visualizes the spatial correlation between the true signals and the expected signals from all test locations  $(x, y)$  [11], [12]. The SAF is expressed as:

$$\mathcal{A}(x, y) = \left| \sum_{n=1}^N \sum_{k=1}^K \mathcal{A}_{nk}(x, y) \right|^2, \quad (14)$$

where

$$\mathcal{A}_{nk}(x, y) = e^{j2\pi \left( \frac{f_c}{c} + \frac{\Delta f}{c} k \right) (d_n(x, y) - d_n)}. \quad (15)$$

When frequency phase offset  $\phi_{nk}^f$  is present, the ambiguity function is expressed as:

$$\mathcal{A}_{nk}^f(x, y) = e^{j2\pi \left( \frac{f_c}{c} + \frac{\Delta f}{c} k \right) (d_n(x, y) - d_n)} \cdot e^{j\phi_{nk}^f}. \quad (16)$$

Similarly, the ambiguity function incorporating spatial phase offset  $\phi_n^a$  is expressed as:

$$\mathcal{A}_{nk}^a(x, y) = e^{j2\pi \left( \frac{f_c}{c} + \frac{\Delta f}{c} k \right) (d_n(x, y) - d_n)} \cdot e^{j\phi_n^a}. \quad (17)$$

We aim to evaluate the ambiguities caused by the phase offsets, which can be revealed by the sidelobe levels in the SAF. Therefore, we define a performance metric named

PMSR, which is the ratio of the SAF peak power to the median sidelobe power:

$$\text{PMSR} = \frac{|\mathcal{A}(x_{\text{sen}}, y_{\text{sen}})|^2}{\text{median}_{(x, y) \in \mathcal{R} \setminus \Omega} |\mathcal{A}(x, y)|^2}, \quad (18)$$

where the SAF peak corresponds to the sensed UE location  $(x_{\text{sen}}, y_{\text{sen}})$ .  $\mathcal{R}$  denotes the full spatial region for evaluating the SAF, and  $\Omega \in \mathcal{R}$  represents the main lobe region. PMSR effectively characterizes the level of the sidelobes in the SAF. The higher PMSR values indicate reduced sidelobe interference, thereby enabling a more accurate localization.

### III. CRAMÉR-RAO LOWER BOUND SIMULATION RESULTS

In this section, we analyze the  $\text{CRLB}_{xy}^{\text{RMSE}}$  derived in Section II-B, under varying levels of frequency and spatial phase offsets. To ensure a meaningful comparison with further real-world validation results, the simulation parameters are aligned with the practical massive MIMO testbed, as described in Section V. The complete list of parameters is summarized in Table I.

#### A. Impact of Frequency Phase Offset

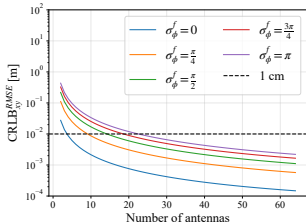
Fig. 3(a) shows the  $\text{CRLB}_{xy}^{\text{RMSE}}$  as a function of the standard deviation  $\sigma_\phi^f$  of the Gaussian-distributed frequency phase offset with different antenna numbers. As  $\sigma_\phi^f$  increases from  $\frac{\pi}{4}$  to  $\pi$ , the  $\text{CRLB}_{xy}^{\text{RMSE}}$  increases by a factor of 5 to 15 compared to the ideal  $\text{CRLB}_{xy}^{\text{RMSE}}$ . This observation indicates that frequency phase distortions, even with large variances, induce only minor degradation in localization accuracy. The robustness against frequency phase offsets arises because such distortions are subcarrier-specific and tend to be averaged out across the multiple subcarriers.

On the other hand, increasing the number of antennas significantly reduces the  $\text{CRLB}_{xy}^{\text{RMSE}}$  due to the enhanced spatial diversity. For example, when a localization accuracy of 1 cm is desired under the presence of  $\sigma_\phi^f = \pi$ , the frequency phase offset does not need to be resolved when using more than 23 antennas. In other words, a preferred localization accuracy can be achieved by either eliminating the frequency phase distortions or using a larger antenna array.

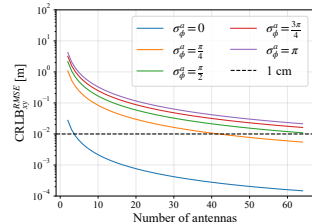
#### B. Impact of Spatial Phase Offset

Fig. 3(b) illustrates the  $\text{CRLB}_{xy}^{\text{RMSE}}$  as a function of the standard deviation  $\sigma_\phi^a$  of the uniformly distributed spatial phase offset. A remarkable increase in the localization error is observed as  $\sigma_\phi^a$  grows. The growth of  $\text{CRLB}_{xy}^{\text{RMSE}}$  is 30 to 130 times compared to the ideal  $\text{CRLB}_{xy}^{\text{RMSE}}$ . This behavior highlights the severe sensitivity of localization performance to spatial phase incoherence. In contrast to frequency phase offset, spatial phase offset directly disrupts the constructive combining of signals across the antenna array.

Moreover, although the  $\text{CRLB}_{xy}^{\text{RMSE}}$  also degrades significantly as the number of antennas increases in this case, a localization accuracy of 1 cm is hard to achieve with a reasonable number of antennas when the spatial phase distortions exist.



(a)



(b)

**Fig. 3:** CRLB-based localization RMSE versus phase incoherence: (a) Frequency phase offset: minor impact on localization accuracy. (b) Spatial phase offset: severe degradation of localization accuracy.

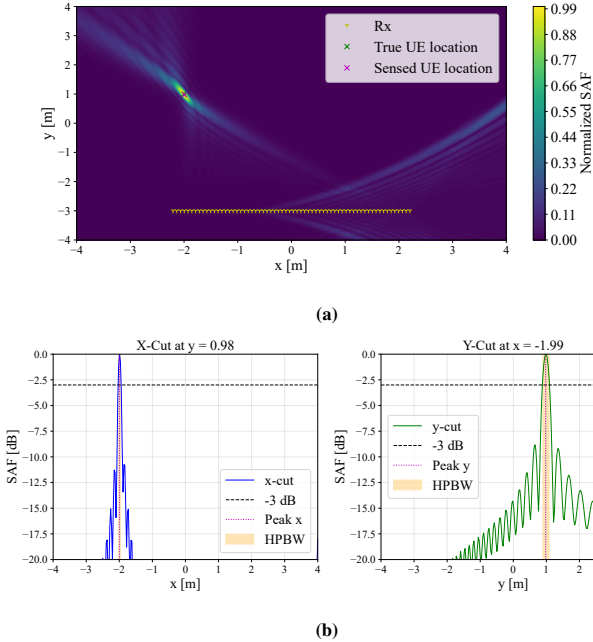


**Fig. 4:** SAF of the simulated ideal signal with  $(x_{\text{true}}, y_{\text{true}}) = (-2, 1)$ : (a) SAF; (b) X- and Y-cuts of the SAF at the sensed UE location. PMSR = 29.45 dB.

#### IV. SPATIAL AMBIGUITY FUNCTION SIMULATION RESULTS

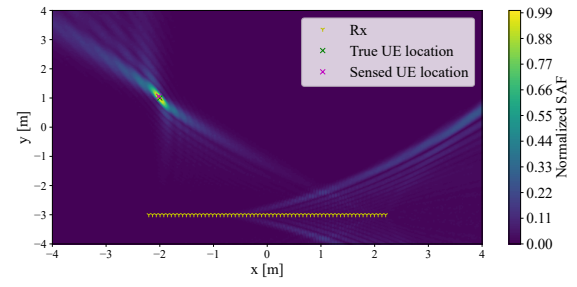
This section presents simulation results of the SAFs and PMSR defined in Section II-C. The simulation parameters follow the practical testbed in Table I as well.

##### A. Spatial Ambiguity Function of Ideal Signal

Fig. 4 presents the SAF computed from the ideal signal model with UE location being  $(x_{\text{true}}, y_{\text{true}}) = (-2, 1)$ . The x- and y-cuts of the SAF are also presented to indicate the sidelobe levels clearly. The SAF exhibits a sharp mainlobe and well-suppressed sidelobes. The high PMSR of 29.45 dB reflects minimal ambiguity.

##### B. Spatial Ambiguity Function with Frequency Phase Offset

To assess the influence of frequency phase offset, we simulate the SAF under varying standard deviation values of the Gaussian-distributed offset. Specifically, we set  $\sigma_{\phi}^f =$



(a)

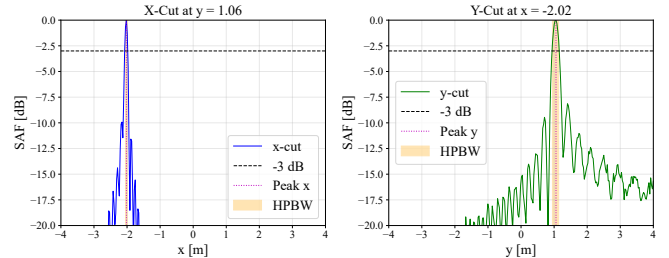


**Fig. 5:** SAF of the simulated signal with frequency phase offset ( $\sigma_{\phi}^f = \frac{\pi}{4}$ ): (a) SAF; (b) X- and Y-cuts of the SAF at the sensed UE location. PMSR = 28.69 dB.

$\{\frac{\pi}{16}, \frac{\pi}{8}, \frac{3\pi}{16}, \frac{\pi}{4}, \frac{5\pi}{16}, \frac{3\pi}{8}, \frac{7\pi}{16}, \frac{\pi}{2}\}$ . Fig. 5 shows one of the resulting SAFs with  $\sigma_{\phi}^f = \frac{\pi}{4}$ . The SAF results reveal that the frequency phase offset has a minor visual impact on the SAF structure. This observation remains consistent with the other values of  $\sigma_{\phi}^f$ . The corresponding trend of PMSR, as plotted in Fig. 7 (blue line), further confirms that the frequency phase offset results in mild variation in localization performance, consistent with CRLB results in Section III-A. This is because the impact tends to average out in matched filtering across the subcarrier dimension.

##### C. Spatial Ambiguity Function with Spatial Phase Offset

Similarly to the frequency phase offset case, we simulate the SAF under varying levels of spatial phase offsets. Fig. 6 presents the resulting SAF with  $\sigma_{\phi}^a = \frac{\pi}{4}$ . Pronounced sidelobe growth is evident, reducing PMSR to 18.48 dB. Unlike frequency phase offset, spatial phase mismatches persist across antennas and directly disrupt coherent signal combination. Fig. 7 (orange line) shows a significant PMSR drop as  $\sigma_{\phi}^a$  increases, mirroring the sharp CRLB degradation seen in Section III-B.

#### V. REAL-WORLD MEASUREMENT VALIDATION

In this section, we apply real-world measurements to validate our theoretical findings. The measured CSI data is processed from a calibration perspective, where frequency and spatial phase offsets are sequentially estimated and compensated using extrinsic calibration with a known UE location.

##### A. Measurement Setup and Data Collection

The practical measurement scenario is shown in Fig. 8. The setup comprises the massive MIMO testbed at KU Leuven and

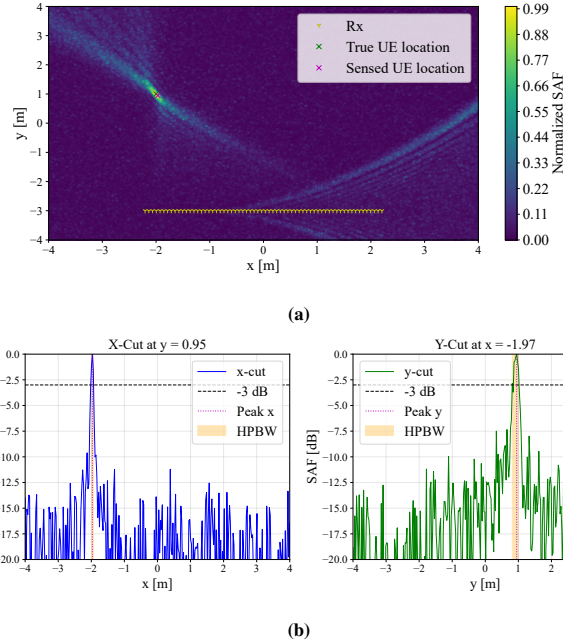


**Fig. 6:** SAF of the simulated signal with spatial phase offset ( $\sigma_{\phi}^a = \frac{\pi}{4}$ ): (a) SAF; (b) X- and Y-cuts of the SAF at the sensed UE location. PMSR = 18.48 dB.

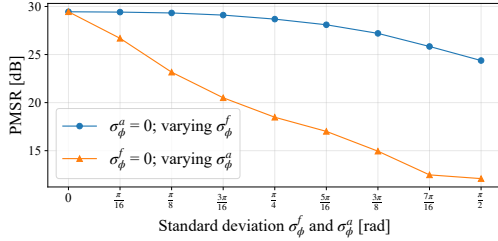


**Fig. 7:** PMSR degradation with increasing frequency phase offset (blue line) and spatial phase offset (orange line).

a Qualisys Motion Capture (MoCap) system [13], [14]. The massive MIMO system operates in time division duplex mode, using OFDM for signal transmission. The UE, equipped with a single dipole antenna, transmits a predefined pilot signal. The base station is equipped with 64 patch antennas arranged as a linear array to receive the pilot signals and perform channel estimation. The detailed system parameters are listed in Table I. To obtain the ground truth location of the UE, the MoCap system is calibrated within the same coordinate system as the MIMO testbed. It provides millimeter-level accuracy measurement by detecting a marker attached to the UE. The CSI data is collected for 5 s, corresponding to  $L = 10000$  OFDM symbols. The resulting measured CSI is represented as  $\mathbf{r} \in \mathbb{C}^{N \times K \times L}$ .

## B. Phase Synchronization Algorithms

### 1) Frequency Phase Offset Estimation and Compensation:

First, the frequency phase offset is estimated using the Least Squares Estimator (LSE). Considering that the UE remains static in a stationary environment, the phase offsets are as-

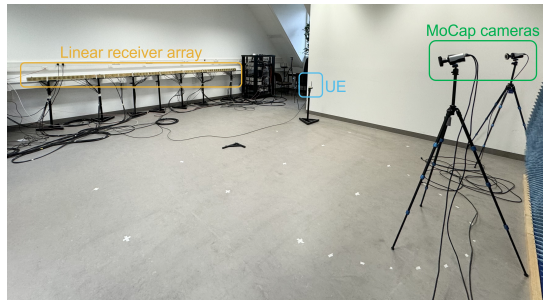


**Fig. 8:** Measurement setup with massive MIMO testbed and motion capture cameras.

**TABLE I:** Massive MIMO system parameters

System parameter	Symbol	Value
Center frequency	$f_c$	3.5 GHz
Bandwidth	BW	18 MHz
Sampling rate	$f_s$	2 kHz
Number of subcarriers	K	100
Subcarrier spacing	$\Delta f$	180 kHz
Number of UE	M	1
Number of receiver antennas	N	64
Antenna spacing	$\Delta a$	0.07 m

sumed to be time-consistent. Therefore, with the ground truth location provided by the MoCap system, the ideal received signal  $r_{nk}(l)$  can be modeled as in (1). Then, the frequency phase offset can be estimated as:

$$\hat{\phi}_{nk}^f = \arg \min_{\phi_{nk}^f} \sum_{l=1}^L \left| \tilde{r}_{nk}(l) - e^{j\phi_{nk}^f} \cdot r_{nk}(l) \right|^2, \quad (19)$$

where  $\tilde{r}_{nk}(l)$  is the measured signal, and  $l = 1, 2, \dots, L$  is the symbol index. The optimal solution of the LSE is given by:

$$e^{j\hat{\phi}_{nk}^f} = \frac{\mathbf{r}_{nk}^H \cdot \tilde{\mathbf{r}}_{nk}}{\mathbf{r}_{nk}^H \cdot \mathbf{r}_{nk}}, \quad (20)$$

where  $(\cdot)^H$  denotes the Hermitian transpose [15]. As a result, the compensated signal can be simply derived as

$$\hat{r}_{nk}(l) = \tilde{r}_{nk}(l) \cdot e^{-j\hat{\phi}_{nk}^f}. \quad (21)$$

### 2) Spatial Phase Offset Estimation and Compensation:

The spatial phase offset is derived and compensated for after performing the matched filter across the subcarrier dimension. Considering the single UE scenario, the peak value along the range dimension is the LoS signal from the UE. As a result of the range processing,  $N$  LoS signals with spatial phase offset calibration are used to compute the localization image, where the phase offset  $e^{j\hat{\phi}_n^a}$  is estimated by comparing the measured signal with the ideal signal  $r_n^{LoS} = e^{-j2\pi\frac{f_c}{c}d_n}$  as:

$$e^{j\hat{\phi}_n^a} = \frac{\tilde{r}_n^{LoS}}{r_n^{LoS}}. \quad (22)$$

Then the compensated signal becomes:

$$\hat{r}_n^{LoS} = \tilde{r}_n^{LoS} \cdot e^{-j\hat{\phi}_n^a}. \quad (23)$$

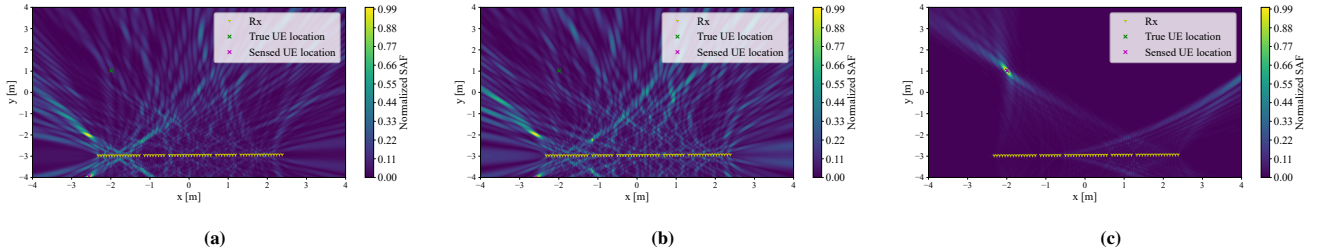


**Fig. 9:** UE localization results: (a) Measured data. (b) After frequency phase offset compensation. (c) After both frequency and spatial offset compensations. PMSR increases from 14.01 dB to 24.95 dB. Localization RMSE reduces from 5 m to 1.2 cm.

### C. Validation Results

#### 1) Localization Performance with Uncalibrated Data:

Fig. 9(a) shows the localization image obtained from uncalibrated CSI data. High sidelobe levels result in a low PMSR of 14.01 dB, making UE localization difficult.

**2) Frequency Phase Offset Compensation Result:** Fig. 9(b) presents the UE localization using the data after frequency phase offset compensation. Compared to Fig. 9(a), compensating frequency phase offset yields minimal improvement in localization performance, which aligns with the theoretical insights in Sections III-A and IV-B.

**3) Spatial Phase Offset Compensation Result:** Fig. 9(c) shows the result after compensation for both frequency and spatial phase offsets. The sidelobes are substantially reduced, with PMSR increasing to 24.95 dB. The UE can be accurately localized, indicating the effectiveness of spatial offset compensation, which also aligns with the simulation results in Sections III-B and IV-C. Notably, the UE localization RMSE reaches 1.2 cm in the real-world scenario.

## VI. CONCLUSION

This paper presents a detailed study of the impact of phase incoherence on OFDM-based massive MIMO systems for localization. We derived the CRLB and developed a unified model that uses the spatial ambiguity function to analyze the effects of frequency-dependent and (spatial) antenna-dependent phase offsets. Our simulation results demonstrated that, in the considered system configuration, frequency offsets have a limited effect on localization performance, whereas spatial offsets significantly degrade localization performance.

To mitigate these effects, we proposed a practical CSI calibration framework that targets both frequency and spatial phase distortions. The proposed method was experimentally validated on a real-world massive MIMO testbed, where we demonstrated its effectiveness in restoring phase coherence and improving localization. Specifically, the localization RMSE was reduced from 5 m to 1.2 cm after calibration, highlighting the critical role of spatial synchronization in localization.

Future work may extend the analytical simulations to wideband systems, where sensitivity to frequency offsets is higher. Additionally, the proposed calibration framework can be adapted for multi-UE and passive target scenarios, providing robust phase synchronization in dynamic environments.

## REFERENCES

- [1] A. Bourdoux, A. N. Barreto, B. van Liempd, C. Lima, D. Dardari, D. Belot, E.-S. Lohan, G. Seco-Granados, H. Sarieddeen, H. Wymeersch, J. Suutala, J. Saloranta, M. Guillaud, M. Isomursu, M. Valkama, M. Aziz, R. Berkvens, T. Sanguanpuak, T. Svensson, and Y. Miao, “6g white paper on localization and sensing,” 06 2020.
- [2] H. Wymeersch and G. Seco-Granados, “Radio localization and sensing—part ii: State-of-the-art and challenges,” *IEEE Communications Letters*, vol. 26, no. 12, pp. 2821–2825, 2022.
- [3] A. Shahmansoori, G. E. Garcia, G. Destino, G. Seco-Granados, and H. Wymeersch, “Position and orientation estimation through millimeter-wave mimo in 5g systems,” *IEEE Transactions on Wireless Communications*, vol. 17, no. 3, pp. 1822–1835, 2018.
- [4] V. Radhakrishnan, O. Taghizadeh, and R. Mathar, “Hardware impairments-aware transceiver design for multi-carrier full-duplex mimo relaying,” *IEEE Transactions on Vehicular Technology*, vol. PP, pp. 1–1, 01 2021.
- [5] C. Studer, M. Wenk, and A. Burg, “Mimo transmission with residual transmit-rf impairments,” in *2010 International ITG Workshop on Smart Antennas (WSA)*, 2010, pp. 189–196.
- [6] C. Li, S. De Bast, E. Tanghe, S. Pollin, and W. Joseph, “Toward fine-grained indoor localization based on massive mimo-ofdm system: Experiment and analysis,” *IEEE Sensors Journal*, vol. 22, no. 6, pp. 5318–5328, 2022.
- [7] P. Moose, “A technique for orthogonal frequency division multiplexing frequency offset correction,” *IEEE Transactions on Communications*, vol. 42, no. 10, pp. 2908–2914, 1994.
- [8] M. Biguesh and A. Gershman, “Training-based mimo channel estimation: a study of estimator tradeoffs and optimal training signals,” *IEEE Transactions on Signal Processing*, vol. 54, no. 3, pp. 884–893, 2006.
- [9] S. Wu and Y. Bar-Ness, “Ofdm systems in the presence of phase noise: consequences and solutions,” *IEEE Transactions on Communications*, vol. 52, no. 11, pp. 1988–1996, 2004.
- [10] Y. Wan, A. Liu, R. Du, T. X. Han, and T. Q. S. Quek, “Fundamental limits and optimization of multiband delay estimation in ofdm systems,” *IEEE Internet of Things Journal*, vol. 11, no. 19, pp. 31112–31127, 2024.
- [11] A. Sakhnini, S. De Bast, M. Guenach, A. Bourdoux, H. Sahli, and S. Pollin, “Near-field coherent radar sensing using a massive mimo communication testbed,” *IEEE Transactions on Wireless Communications*, vol. 21, no. 8, pp. 6256–6270, 2022.
- [12] M. Manzoni, D. Tagliaferri, S. Tebaldini, M. Mizmizi, A. V. Monti-Guarnieri, C. M. Prati, and U. Spagnolini, “Wavefield networked sensing: Principles, algorithms, and applications,” *IEEE Open Journal of the Communications Society*, vol. 6, pp. 181–197, 2025.
- [13] NI, “5g massive mimo testbed: From theory to reality,” 2. [Online]. Available: <http://www.ni.com/nl-be/innovations/white-papers/14/5g-massivemimo-testbedfrom-theory-to-reality.html>
- [14] Qualisys, “Miqus,” 2. [Online]. Available: [https://cdn-content.qualisys.com/2020/01/PI\\_Miqus.pdf](https://cdn-content.qualisys.com/2020/01/PI_Miqus.pdf)
- [15] *Fundamentals of Statistical Signal Processing, Volume 1: Estimation Theory*. Pearson Education. [Online]. Available: <https://books.google.be/books?id=pDnV5qf1f6IC>